Numerical studies of isotopic selective photoionization of ytterbium in a three-step ionization scheme

Xiao-Yong Lu(卢肖勇)[†] and Li-De Wang(王立德)

Science and Technology on Particle Transport and Separation Laboratory, CNNC, Tianjin 300180, *China*

(Received 7 June 2022; revised manuscript received 2 October 2022; accepted manuscript online 19 October 2022)

Selective photoionization of ytterbium isotope is studied numerically based on a three-step photoionization scheme, $4f^{14}6s^2\ {}^1S_0$ (0 cm^{-1}) $\rightarrow$ $4f^{14}6s6p\ {}^3P_1$ (17992.008 cm^{-1}) $\rightarrow$ $(4f^{13}6s^26p)\ (7/2,\ 3/2)_2$ (35196.98 cm^{-1}) $\rightarrow$ auto-ionization state (52353 cm^{-1}) $\rightarrow$ Yb^+, by the density matrix theory with the consideration of atomic hyperfine structures and magnetic sublevels. To examine the physical model, the numerical isotopic abundance of ytterbium is compared with that from mass spectroscopy experiment, showing that they are in good agreement with each other. The excitation process and ionization process of ytterbium, especially for odd isotopes, are discussed and analyzed in detail on this basis. The effects of frequency detuning, power densities, spectral bandwidths, polarization of two excitation lasers, and atomic Doppler broadening on the total ionization yield and isotopic abundance are investigated numerically and the optimal excitation conditions for ^{176}Yb enrichment are identified semi-quantitatively.

Keywords: ytterbium isotope, hyperfine structure, selective photoionization

PACS: 32.80.–t, 32.80.Rm, 42.50.Hz **DOI:** 10.1088/1674-1056/ac9b2f

1. Introduction

Lanthanide isotopes, either stable or radioactive, are widely used in scientific research, industrial production, nuclear engineering, and medical treatments.[1,2] Taking stable lanthanide isotopes for example, ^{150}Nd is a candidate nuclide for studying neutrinoless double beta decay.[3] ^{168}Yb can be used to produce ^{169}Yb, which is more appropriate for industrial non-destructive testing than ^{60}Co and ^{192}Ir due to its relatively low-energy gamma ray.[4] ^{146}Nd can serve as the target material of neutron irradiation to produce ^{147}Pm, which is a fuel of radioisotope battery.[5] ^{157}Gd, ^{164}Dy, and ^{167}Er can be incorporated into burnable poisons in nuclear reactors due to their large capture cross sections for thermal neutrons.

It is worth noting that lanthanide radioisotopes have attracted much attention in medical diagnosis and targeted radionuclide therapy (TRT), and they are usually produced by the irradiation of enriched stable isotopes in reactors or accelerators.[6–8] Especially, ^{177}Lu is an important radioisotope in medical applications for its decay properties. ^{177}Lu decays to the excited (24%) or ground (76%) state ^{177}Hf by β-radiation, with the maximum energy of 497.1 keV and a half-life of 6.65 days.[9] The excited ^{177}Hf decays to its ground state by emitting γ-radiation with energy of 112.95 keV and 208.37 keV subsequently.[9] The soft β-radiation can mitigate undesirable exposes to healthy tissues, and the low-energy γ-radiation is beneficial to lesion imaging and dosimetry assessment. Although radio-pharmaceuticals containing ^{177}Lu have emerged and boomed recently, their large-scale applications are limited by the global production capacity of ^{177}Lu. There are two mainstream production routes for ^{177}Lu, namely neutron irradiation of enriched ^{176}Yb (Yb-route) or enriched ^{176}Lu (Lu-route).[9–12] In the Lu-route, the metastable isomer ^{177m}Lu with a half-life of 160.1 days is coproduced in trace quantities. It is hard to extract desirable ^{177}Lu from the ^{176}Lu carrier and ^{177m}Lu impurity by chemical methods, causing a detriment to product's specific radioactivity and increasing the difficulty in managing medical waste.[13] By contrast, the Yb-route can produce the non-carrier added ^{177}Lu without ^{177m}Lu, showing more popularity among researchers and manufacturers (like SHINE Medical Technologies in America, Bruce Power in Canada, Isotope Technologies Munich in Germany, Nuclear Research and Consultancy Group in Netherlands, and so on) and fueling the demand for enriched ^{176}Yb. Isotope separation of ytterbium cannot be realized through the centrifugation method because ytterbium does not have any volatile compounds. The electromagnetic separation method is feasible theoretically, but its cost is too high. As a result, the laser isotope separation (LIS) method is the only option for economic ytterbium isotope separation.[14–18]

Basically, the LIS method is based on isotopic selective photoionization of atomic vapors under several narrow-bandwidth laser pulses. Target isotopes are excited and ionized resonantly, while non-target isotopes are ionized barely due to the isotope shifts. It is worth noting that hyperfine structures have significant influences on the effective isotope shift because some components in the hyperfine structure may be closer to the fine energy levels of other isotopes than the center of gravity. Accordingly, two critical indices of LIS process, namely total ionization yield and target isotope abundance, display larger variations than those under the hypothetical condition of no hyperfine structures. Besides, the transition strengths between different magnetic sublevels, which

[†]Corresponding author. E-mail: lu-xy15@tsinghua.org.cn

© 2023 Chinese Physical Society and IOP Publishing Ltd

are controlled by transition selection rules and laser polarization, also affect the excitation process and ionization process. Consequently, apart from the common parameters such as laser bandwidth and atomic Doppler broadening, the hyperfine structures and magnetic sublevels should be considered in ytterbium photoionization numerical studies.

In this work, the isotopic selective photoionization of ytterbium is studied numerically under a three-step photoionization scheme, $4f^{14}6s^2\ {}^1S_0$ (0 cm^{-1}) $\rightarrow$ $4f^{14}6s6p\ {}^3P_1$ (17992.008 cm^{-1}) $\rightarrow$ $(4f^{13}6s^26p)\ (7/2, 3/2)_2$ (35196.98 cm^{-1}) $\rightarrow$ auto-ionization state (52353 cm^{-1}) $\rightarrow$ Yb^+. First, a general theoretical model for three-step photoionization process is proposed based on the density matrix theory, with hyperfine structures and magnetic sublevels taken into consideration. Then, properties of excitation process and ionization process are discussed and analyzed after being compared with experimental results. Next, efficient and selective photoionization processes to enrich ^{176}Yb are optimized. Finally, some conclusions are are drawn from the present studies.

2. Theoretical model

Generally, the coherent interaction of atomic vapors with lasers in LIS process is equivalent to that of an individual atom with lasers. Figure 1 shows the schematic diagram of ytterbium three-step photoionization process. The ground state $|1\rangle$, the first excited state $|2\rangle$, and the second excited state $|3\rangle$ split into sublevels $|1,i\rangle$, $|2,j\rangle$, and $|3,k\rangle$ respectively. Each sublevel represents a magnetic sublevel rather than a hyperfine structure ensemble. The wave function $\boldsymbol{\Psi}$ of an individual atom can be considered as the superposition of sublevels under the excitation of lasers, and expressed as

$$\boldsymbol{\Psi} = \sum_i a_1(i)\boldsymbol{\Phi}_1(i) + \sum_j a_2(j)\boldsymbol{\Phi}_2(j) + \sum_k a_3(k)\boldsymbol{\Phi}_3(k), \quad (1)$$

where $\boldsymbol{\Phi}_1(i)$ and $a_1(i)$ are the eigenfunction and probability amplitude of sublevel $|1,i\rangle$ respectively.

In the electric dipole approximation, rotating-wave approximation (RWA) and adiabatic approximation,[19,20] the temporal evolutions of probability amplitudes are written as

$$\frac{\mathrm{d}}{\mathrm{d}t}a_1(i) = \frac{\mathrm{i}}{2}\sum_{j=1}^{J}\Omega_1(i,j)a_2(j)\,\mathrm{e}^{\mathrm{i}\Delta_{12}(i,j)t}, \quad (2a)$$

$$\frac{\mathrm{d}}{\mathrm{d}t}a_2(j) = \frac{\mathrm{i}}{2}\sum_{k=1}^{K}\Omega_2(j,k)a_3(k)\,\mathrm{e}^{\mathrm{i}\Delta_{23}(j,k)t} + \frac{\mathrm{i}}{2}\sum_{i=1}^{I}\Omega_1^*(i,j)a_1(i)\,\mathrm{e}^{-\mathrm{i}\Delta_{12}(i,j)t}, \quad (2b)$$

$$\frac{\mathrm{d}}{\mathrm{d}t}a_3(k) = \frac{\mathrm{i}}{2}\sum_{j=1}^{J}\Omega_2^*(j,k)a_2(j)\,\mathrm{e}^{-\mathrm{i}\Delta_{23}(j,k)t}, \quad (2c)$$

where i is the imaginary unit; I, J, and K are the total sublevel numbers of the ground, the first, and the second excited states respectively; $\Delta_{12}(i,j)$ is the frequency detuning between the first laser and the transition $|1,i\rangle \rightarrow |2,j\rangle$, $\Omega_1(i,j)$ is the corresponding Rabi frequency. Similarly, $\Delta_{23}(j,k)$ and $\Omega_2(j,k)$ are the frequency detuning between the second laser and the transition $|2,j\rangle \rightarrow |3,k\rangle$, and the corresponding Rabi frequency.

Probability amplitudes of sublevels are replaced by density matrix elements $\rho_{mn}(m',n') = a_m(m')\cdot a_n^*(n')$ for convenience, where diagonal elements $\rho_{11}(i,i)$, $\rho_{22}(j,j)$, and $\rho_{33}(k,k)$ are the population probability of sublevels $|1,i\rangle$, $|2,j\rangle$, and $|3,k\rangle$ respectively. Off-diagonal elements describe the coherence degree between two corresponding sublevels, and ρ_{ion} is the ionization probability. Based on the above equations, the relaxation processes of excited states are introduced as a product of the relaxation rate and density matrix element. The time-varying equations are shown as follows:

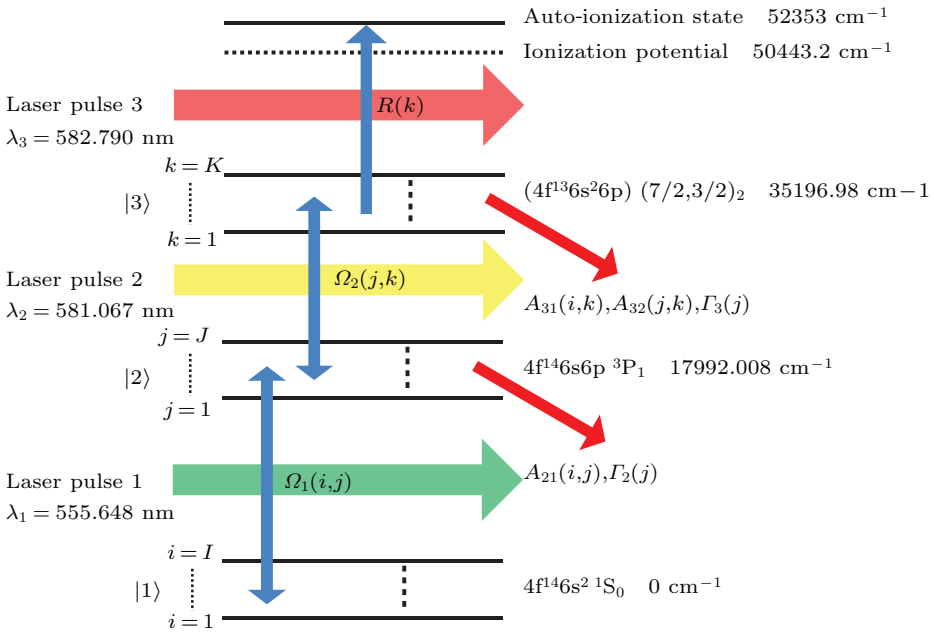


Fig. 1. Schematic diagram of ytterbium three-step photoionization processes.

$$\frac{\mathrm{d}}{\mathrm{d}t}\rho_{11}(i,i') = \frac{\mathrm{i}}{2}\sum_{j=1}^{J}\Omega_1(i,j)\rho_{12}^*(i',j)\,\mathrm{e}^{\mathrm{i}\Delta_{12}(i,j)t} - \frac{\mathrm{i}}{2}\sum_{j=1}^{J}\Omega_1^*(i',j)\rho_{12}(i,j)\,\mathrm{e}^{-\mathrm{i}\Delta_{12}(i',j)t} + \delta_{i,i'}\sum_{j=1}^{J}A_{21}(i,j)\rho_{22}(j,j), \tag{3a}$$

$$\begin{aligned}\frac{\mathrm{d}}{\mathrm{d}t}\rho_{22}(j,j') = {}& \frac{\mathrm{i}}{2}\sum_{k=1}^{K}\Omega_2(j,k)\rho_{23}^*(j',k)\,\mathrm{e}^{\mathrm{i}\Delta_{23}(j,k)t} + \frac{\mathrm{i}}{2}\sum_{i=1}^{I}\Omega_1^*(i,j)\rho_{12}(i,j')\,\mathrm{e}^{-\mathrm{i}\Delta_{12}(i,j)t}\\ & - \frac{\mathrm{i}}{2}\sum_{k=1}^{K}\Omega_2^*(j',k)\rho_{23}(j,k)\,\mathrm{e}^{-\mathrm{i}\Delta_{23}(j',k)t} - \frac{\mathrm{i}}{2}\sum_{i=1}^{I}\Omega_1(i,j')\rho_{12}^*(i,j)\,\mathrm{e}^{\mathrm{i}\Delta_{12}(i,j')t}\\ & - \frac{1}{2}\left(\sum_{i=1}^{I}A_{21}(i,j) + \sum_{i=1}^{I}A_{21}(i,j') + \Gamma_2(j) + \Gamma_2(j')\right)\rho_{22}(j,j') + \delta_{j,j'}\sum_{k=1}^{K}A_{32}(j,k)\rho_{33}(k,k),\end{aligned} \tag{3b}$$

$$\begin{aligned}\frac{\mathrm{d}}{\mathrm{d}t}\rho_{33}(k,k') = {}& \frac{\mathrm{i}}{2}\sum_{j=1}^{J}\Omega_2^*(j,k)\rho_{23}(j,k')\,\mathrm{e}^{-\mathrm{i}\Delta_{23}(j,k)t} - \frac{\mathrm{i}}{2}\sum_{j=1}^{J}\Omega_2(j,k')\rho_{23}^*(j,k)\,\mathrm{e}^{\mathrm{i}\Delta_{23}(j,k')t}\\ & - \frac{1}{2}\left[\sum_{j=1}^{J}A_{32}(j,k) + \sum_{j=1}^{J}A_{32}(j,k') + \Gamma_3(k) + \Gamma_3(k') + R(k) + R(k')\right]\rho_{33}(k,k'),\end{aligned} \tag{3c}$$

$$\frac{\mathrm{d}}{\mathrm{d}t}\rho_{\mathrm{ion}} = \sum_{k=1}^{K}R(k)\rho_{33}(k,k), \tag{3d}$$

$$\begin{aligned}\frac{\mathrm{d}}{\mathrm{d}t}\rho_{12}(i,j) = {}& \frac{\mathrm{i}}{2}\sum_{j'=1}^{J}\Omega_1(i,j')\rho_{22}(j',j)\mathrm{e}^{\mathrm{i}\Delta_{12}(i,j')t} - \frac{\mathrm{i}}{2}\sum_{i'=1}^{I}\Omega_1(i',j)\rho_{11}(i,i')\mathrm{e}^{\mathrm{i}\Delta_{12}(i',j)t}\\ & - \frac{\mathrm{i}}{2}\sum_{k'=1}^{K}\Omega_2^*(j,k')\rho_{13}(i,k')\mathrm{e}^{-\mathrm{i}\Delta_{23}(j,k')t} - \frac{1}{2}\left(\sum_{i=1}^{I}A_{21}(i,j) + \Gamma_2(j) + 2b_1\frac{\beta_1^2b_1^2}{\Delta_1^2+\beta_1^2b_1^2}\right)\rho_{12}(i,j),\end{aligned} \tag{3e}$$

$$\begin{aligned}\frac{\mathrm{d}}{\mathrm{d}t}\rho_{13}(i,k) = {}& \frac{\mathrm{i}}{2}\sum_{j'=1}^{J}\Omega_1(i,j')\rho_{23}(j',k)\mathrm{e}^{\mathrm{i}\Delta_{12}(i,j')t} - \frac{\mathrm{i}}{2}\sum_{j'=1}^{J}\Omega_2(j',k)\rho_{12}(i,j')\mathrm{e}^{\mathrm{i}\Delta_{23}(j',k)t}\\ & - \frac{1}{2}\left(\sum_{j=1}^{J}A_{32}(j,k) + \Gamma_2(j) + \Gamma_3(k) + 2b_1\frac{\beta_1^2b_1^2}{\Delta_1^2+\beta_1^2b_1^2} + 2b_2\frac{\beta_2^2b_2^2}{\Delta_2^2+\beta_2^2b_2^2}\right)\rho_{13}(i,k),\end{aligned} \tag{3f}$$

$$\begin{aligned}\frac{\mathrm{d}}{\mathrm{d}t}\rho_{23}(j,k) = {}& \frac{\mathrm{i}}{2}\sum_{k'=1}^{K}\Omega_2(j,k')\rho_{33}(k',k)\mathrm{e}^{\mathrm{i}\Delta_{23}(j,k')t} - \frac{\mathrm{i}}{2}\sum_{j'=1}^{J}\Omega_2(j',k)\rho_{22}(j,j')\mathrm{e}^{\mathrm{i}\Delta_{23}(j',k)t}\\ & + \frac{\mathrm{i}}{2}\sum_{i'=1}^{I}\Omega_1^*(i',j)\rho_{13}(i',k)\mathrm{e}^{-\mathrm{i}\Delta_{12}(i',j)t}\\ & - \frac{1}{2}\left(\sum_{i=1}^{I}A_{21}(i,j) + \sum_{j=1}^{J}A_{32}(j,k) + \Gamma_2(j) + \Gamma_3(k) + R(k) + 2b_2\frac{\beta_2^2b_2^2}{\Delta_2^2+\beta_2^2b_2^2}\right)\rho_{23}(j,k).\end{aligned} \tag{3g}$$

These equations can be rewritten into a compact form $\frac{\mathrm{d}}{\mathrm{d}t}\boldsymbol{\rho} = \boldsymbol{Q}\cdot\boldsymbol{\rho}$, where

$$\begin{aligned}\boldsymbol{\rho} = {}& [\rho_{11}(i,i),\rho_{22}(j,j),\rho_{33}(k,k),\rho_{\mathrm{ion}},\rho_{12}(i,j),\\ & \rho_{13}(i,k),\rho_{23}(j,k)]^{\mathrm{T}}\end{aligned}$$

and $\boldsymbol{Q}$ is the density matrix. The total number of complex equations is $(I\times I+J\times J+K\times K+1+I\times J+I\times K+J\times K)$, *i.e.*, 59, 233, and 2089 for even ytterbium isotopes, ^{171}Yb and ^{173}Yb respectively.

The Rabi frequencies $\Omega_1(i,j)$ and $\Omega_2(j,k)$ are defined as

$$\begin{aligned}\Omega_1(i,j) &= \frac{\langle J_1,F_1,m_1|d_{12}|J_2,F_2,m_2\rangle E_1}{\hbar},\\ \Omega_2(j,k) &= \frac{\langle J_2,F_2,m_2|d_{23}|J_3,F_3,m_3\rangle E_2}{\hbar},\end{aligned} \tag{4}$$

where E_1 and E_2 are the slowly varying amplitudes of laser fields; $\langle J_1,F_1,m_1|d_{12}|J_2,F_2,m_2\rangle$ and $\langle J_2,F_2,m_2|d_{23}|J_3,F_3,m_3\rangle$ are the electric dipole moment matrix elements between atomic magnetic sublevels; $\hbar$ is the reduced Planck constant.

The laser power density P for quasi-monochromatic laser field is written as follows:

$$P = \frac{1}{2}c\varepsilon_0E^2, \tag{5}$$

where c and ε are the light speed and permittivity in vacuum, respectively.

The electric dipole moment matrix element between atomic magnetic sublevels is obtained to be

$$\begin{aligned}&\frac{\langle J',F',m'|d|J'',F'',m''\rangle}{\langle J'|d|J''\rangle}\\ &= (-1)^{J'+I_{\mathrm{n}}+2F'-m'}\sqrt{(2F'+1)(2F''+1)}\delta_{m'-m'',\lambda}\\ &\quad\times\begin{Bmatrix} J' & F' & I_{\mathrm{n}}\\ F'' & J'' & 1\end{Bmatrix}\begin{pmatrix} F' & 1 & F''\\ -m' & \lambda & m''\end{pmatrix},\end{aligned} \tag{6}$$

where $\langle J'|d|J''\rangle$ is the reduced matrix element between two fine structures, which is the same value for different isotopes;[21] $\{\ \}$ and $(\ )$ are the Wigner 6-j symbol and Wigner 3-j symbol, respectively; J', F', and m' are the electronic angular momentum quantum number, atomic angular momentum quantum number, and magnetic quantum number of the lower sub-state, respectively; J'', F'', and m'' are the corresponding quantum numbers of the upper sub-state; I_n is the nuclear spin; δ is Kronecker delta function; $\lambda = 0$ and ± 1 represent the linearly polarized laser and circularly polarized laser, respectively. The schematic diagram of transition rules between magnetic sublevels is shown in Fig. 2.

The relaxation of $|2,j\rangle$ includes two parts, *i.e.*, $A_{21}(i,j)$ and $\Gamma_2(j)$, which are the spontaneous radiation rate from $|2,j\rangle$ to $|1,i\rangle$ and to other states, respectively. $A_{32}(j,k)$ and $\Gamma_3(k)$ are the corresponding relaxation rate from $|3,k\rangle$ to $|2,j\rangle$ and other states respectively. Generally, the auto-ionization state is selected as the terminal state for effective ionization in the three-step photoionization scheme. Since the auto-ionization process involves multi-electron excitation, which is beyond the range of application of the semi-classical theory, the auto-ionization rate $R(k)$ is introduced into the theoretical model, as shown in Eq. (3). The $R(k)$ is proportional to the photoionization cross section $\sigma_{\rm ion}$ and flux density of the third laser ϕ, and they are related by the following equation:

$$R(k) = \sigma_{\rm ion}\phi. \tag{7}$$

The laser bandwidth is introduced according to the phase diffusion model as $2b\frac{\beta^2 b^2}{\Delta^2+\beta^2 b^2}$ in Eq. (3), where $2b$ is the full width at half maximum (FWHM) bandwidth, β is the dimensionless cut-off coefficient, Δ is the frequency detuning. In phase diffusion model, the laser spectrum displays a Lorentzian profile near the central wavelength, but turns to quasi-monochrome when Δ is far larger than $2b$. The laser spectrum can be adjusted by the cut-off coefficient β in numerical simulations. In the following simulations, the cut-off coefficients of the first two lasers are set to the same value.

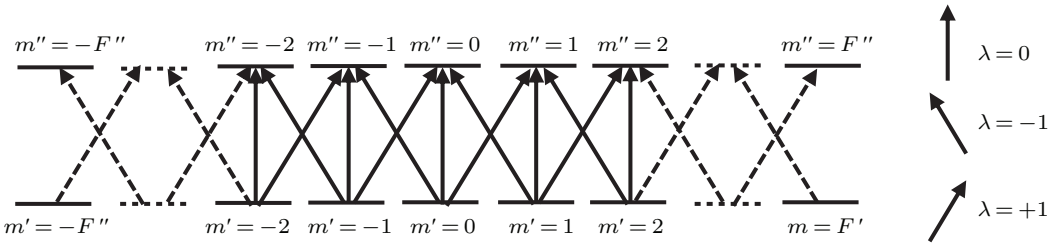


Fig. 2. Schematic diagram of transition rules between magnetic sublevels.

The total ionization yield $P_{\rm ion}$, which is defined as the weighted average value of ionization probabilities of all isotopes, and written as

$$P_{\rm ion} = \sum_p C_p \rho_{{\rm ion},p}, \tag{8}$$

where $\rho_{{\rm ion},p}$ and C_p are the ionization probability and natural abundance of isotope p respectively.

3. Results and discussion

Based on the dye oscillators and amplifiers, the three-step photoionization scheme, $4f^{14}6s^2\ ^1S_0$ (0 cm^{-1}) $\rightarrow$ $4f^{14}6s6p\ ^3P_1$ (17992.008 cm^{-1}) $\rightarrow$ ($4f^{13}6s^26p$) (7/2, 3/2)$_2$ (35196.98 cm^{-1}) $\rightarrow$ auto-ionization state (52353 cm^{-1}) $\rightarrow$ Yb^+, is adopted in this work. This three-step photoionization scheme was also used to conduct the Yb LIS experiments by other researchers.[14–18] The natural abundances, nuclear spins and isotope shifts of ytterbium isotopes are list in Table 1, where all of the isotope shifts are relative to ^{176}Yb, and the number in bracket is the atomic angular momentum quantum number. All even isotopes do not have hyperfine splitting, while ^{171}Yb and ^{173}Yb with non-zero nuclear spins own hyperfine structures for both excited states.[22]

Table 1. Natural abundances, nuclear spin, and isotope shifts of ytterbium isotopes.

Isotope	^{168}Yb	^{170}Yb	^{171}Yb	^{172}Yb	^{173}Yb	^{174}Yb	^{176}Yb
Natural abundance (%)	0.14	3.03	14.31	21.82	16.13	31.84	12.73
Nuclear spin			1/2		5/2		
Isotope shift of the first excited state (GHz)	4.612	3.242	–1.177(1/2) 4.762(3/2)	1.955	4.762(3/2) 3.267(5/2) –1.432(7/2)	0.954	
Isotope shift of the second excited state (GHz)	–8.259	–5.655	–6.617(3/2) –3.789(5/2)	–3.334	–1.963(1/2) –1.428(3/2) –1.118(5/2) –1.840(7/2) –4.743(9/2)	–1.624	

Based on the measurement of excited state lifetimes and spectral linewidths in Ref. [23], the reduced matrix elements $\langle J'|d|J''\rangle$ of the first transition and the second transition are set to 4.66×10^{-30} C·m and 1.15×10^{-30} C·m respectively.[20,22] The photoionization cross section σ_{ion} is taken as 6.7×10^{-20} m^2 for the entire hyperfine structures of the second excited state.[23] The lifetimes of the first and second excited states are 840 ns and 1120 ns respectively.[23] The fourth-order Runge–Kutta algorithm is adopted in simulations, and the time step is set to 0.01 ns for accuracy. Initially, all the atoms populate at the ground state.

3.1. Comparison with experimental data

Aiming at the selective photoionization of ^{168}Yb and ^{176}Yb, the results of the theoretical model are compared with experimental data.[17,18,24] In experiment, ytterbium atoms are first excited by two single-mode dye lasers and then ionized by a broadband dye laser. The isotope abundance of ytterbium ions is tested by a time-of-flight mass spectrometer. The bandwidths of three lasers are 0.25 GHz, 0.25 GHz, and 6.0 GHz, respectively. Other experimental parameters can refer to Park *et al.*'s work.[24] The ratios of linearly polarized component to left-circularly polarized component to right-circularly polarization polarized component in two excitation laser pulses, which are demonstrated to have negligible influences on selective photoionization of ytterbium in Subsection 3.3, will be both set to 1:1:1 in numerical simulations. Ytterbium atoms are assumed to be static in the laser propagation direction.

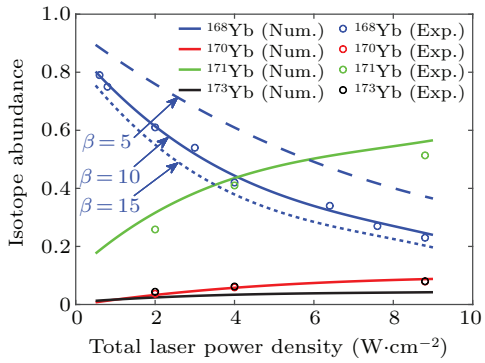


Fig. 3. Experimental and numerical abundances of ytterbium isotopes *versus* total laser power density, with power density ratio of three lasers maintained at 1:2:5, consistent with that in Ref. [24].

Figure 3 shows the experimental and numerical simulated ytterbium isotope abundances *versus* total laser power density. In measurement, the power density ratio of three lasers is maintained at 1:2:5 and laser frequencies are resonant with the resonance frequency of ^{168}Yb.[24] The abundance of ^{172}Yb, ^{174}Yb, and ^{176}Yb are not presented in Fig. 3 because these signals are too small to be observed in experiment. Because the experimental laser frequency spectrum is unknown, ^{168}Yb abundances are calculated with different values of cut-off coefficient β in the phase diffusion model as shown by the three blue lines. The $\beta = 10$ indicated by the blue solid line is selected in the following simulations according to the smallest errors between numerical and experimental values. Indicated by the four solid lines, the experimental and numerical results show that they are in reasonable agreement for the four measurable ytterbium isotopes when the total laser power density changes from 0.6 W/cm^2 to 8.8 W/cm^2.

Figure 4 shows the numerical abundances of ^{176}Yb and ^{168}Yb *versus* the total laser power density when the power densities ratio is maintained at 1:2:25. In experiment, the abundances of ^{176}Yb and ^{168}Yb reach more than 99.5% and 90% when laser frequencies are tuned to the frequencies resonant with ^{176}Yb and ^{168}Yb respectively under a specific total laser power density.[17] Because the total power density is not provided in the reference, it can be inferred that the numerical abundances of ^{176}Yb and ^{168}Yb are well consistent with experimental data at two different resonant frequencies if the total power density is set to 0.5 W/cm^2.

The testing results for these two cases show that the theoretical model shown by Eq. (3) is credible, and excitation mechanisms and optimal excitation conditions of ^{176}Yb enrichment can be found without lots of troublesome experiments.

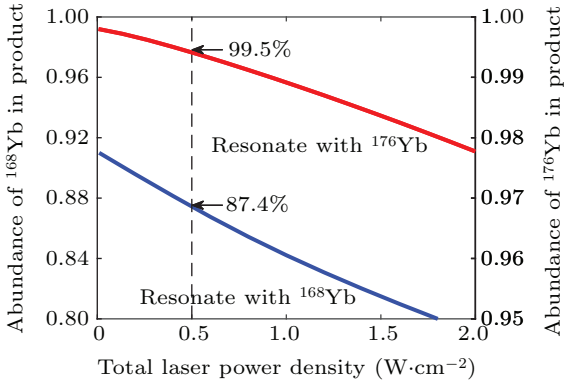


Fig. 4. Numerical abundances of ytterbium isotopes *versus* total laser power density, with power densities ratio of three lasers maintained at 1:2:25, consistent with that in Ref. [17].

3.2. Photoionization properties

The interactions between ytterbium atoms and lasers are simulated and discussed in this subsection. Laser parameters in simulations are listed in Table 2. The saturated power densities of the first laser and the second laser, which are 0.06 W/cm^2 and 2.2 W/cm^2 respectively, are selected for effective excitation. Under the combination of these saturated laser power densities, the ionization probability of even ytterbium isotope decreases to 90% of the saturated value when one laser is kept at the saturated power density and another is set to 50% saturated power density. Experimental laser bandwidths and pulse widths used in Subsection 3.1 are still adopted in following simulations.[24] The FWHM of 52353 cm^{-1} autoionization state is generally much greater than the isotope shifts and hyperfine splitting of the second excited state, thus the bandwidth and polarization of the third laser are not presented. Ytterbium atoms are assumed to be static in the laser propagation direction and simulation parameters remain unchanged as indicated in Table 2 unless otherwise specified.

Table 2. Laser parameters in ytterbium photoionization simulations.

Laser parameter	The first laser	The second laser	The thirrd laser
Power density (W·cm^{-2})	0.06	2.2	5.0
FWHM pulse width (ns)	10	10	10
FWHM bandwidth (GHz)	0.25	0.25	–
Polarization	1:1:1	1:1:1	–

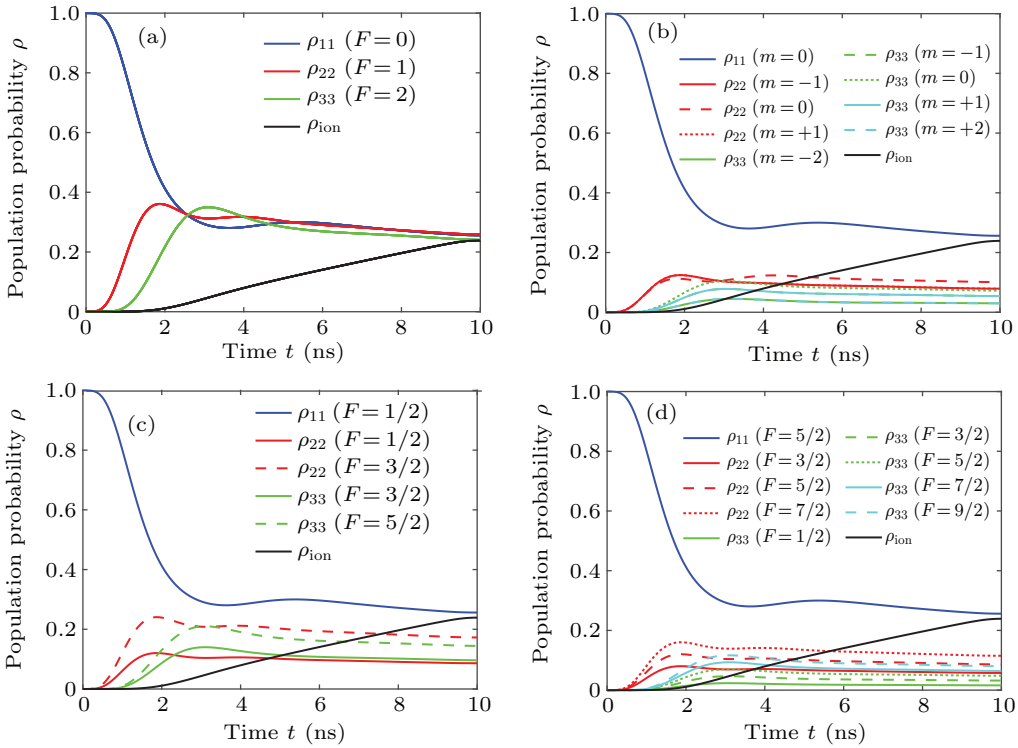


Fig. 5. Population dynamics of several ytterbium isotopes under the assumption of zero hyperfine splitting. (a) ^{176}Yb ($I_{\rm n}=0$), (b) ^{176}Yb ($I_{\rm n}=0$, magnetic sublevels), (c) ^{171}Yb ($I_{\rm n}=1/2$, hyperfine levels), (d) ^{173}Yb ($I_{\rm n}=5/2$, hyperfine levels).

Firstly, a hypothetical case, in which the hyperfine splittings of two excited states are both set to zero for odd isotopes, is presented. The population dynamics of ^{176}Yb, ^{171}Yb, and ^{173}Yb under resonant excitation are shown in Fig. 5, where figure 5(a) indicates the population dynamics of ^{176}Yb's fine levels, figure 5(b) indicates those of ^{176}Yb's magnetic sublevels, figures 5(c) and 5(d) exhibit those of odd isotopes' hyperfine levels. The population of each level and ionization probability display the same characteristics over time even though nuclear spins of three isotopes are different. Moreover, this property is not influenced by laser parameters in simulations, such as the power density, frequency detuning, bandwidth, and polarization, indicating that the excitation process and ionization process of isotopes are not disturbed by nuclear spin under the hypothetical condition of zero hyperfine splitting.

Figures 6–8 show the two-dimensional contour plots of ionization probabilities of ^{176}Yb, ^{171}Yb, and ^{173}Yb isotopes *versus* frequency detuning respectively, where the hyperfine structures of odd isotopes are set to actual values as indicated in Table 1. The results of other even isotopes are not presented because they can be obtained easily by translating Fig. 6 according to isotope shifts. Frequency detuning is set to zero when both two excitation lasers resonate with ^{176}Yb isotope. The central wavelengths of even isotopes, ^{171}Yb and ^{173}Yb are marked by black, red, and blue circles respectively in the three figures, with the sequential change of F values marked for odd isotopes. It can be inferred from the simulation results that (i) the peak ionization probabilities of several transition

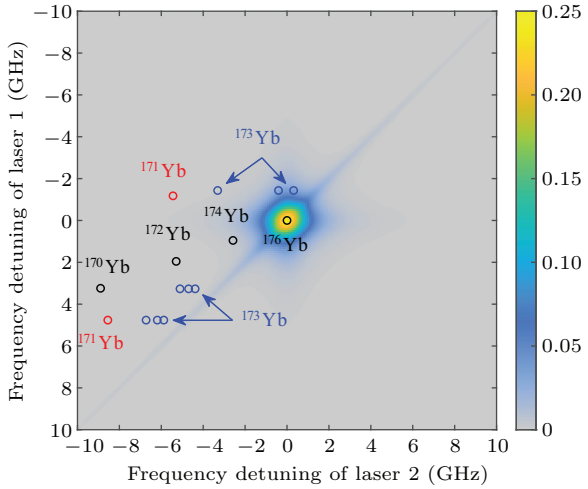


Fig. 6. Two-dimensional contour plot of ^{176}Yb ionization probability *versus* frequency detuning.

channels are quite different for odd ytterbium isotopes; (ii) the peak ionization probabilities of even ytterbium isotope, ^{171}Yb and ^{173}Yb are quite different under the same excitation parameters, and the ordering of peak ionization probabilities depend on laser power density.

The first phenomenon can be explained as follows. According to the Wigner 6-j symbol, the reduced matrix element redistributes unequally among different transition channels for odd isotopes. Inevitably, some paths manifest themselves as strong peaks with larger ionization probability while others are faint. The wider ionization probability distribution represents higher transition strength in the two-dimensional contour plot of ionization probability. These phenomena are shown by the distribution of ^{171}Yb ionization probability evidently in Fig. 7. The transition strength of $F = 1/2 \rightarrow 1/2$ is weaker than that of $F = 1/2 \rightarrow 3/2$ in the first transition, and the transition strength of $F = 3/2 \rightarrow 3/2$ is weaker than that of $F = 1/2 \rightarrow 3/2$ and $F = 3/2 \rightarrow 5/2$ in the second transition. Identical phenomena can be observed in ^{173}Yb ionization process despite more complex hyperfine structures and tinier energy level spacing.

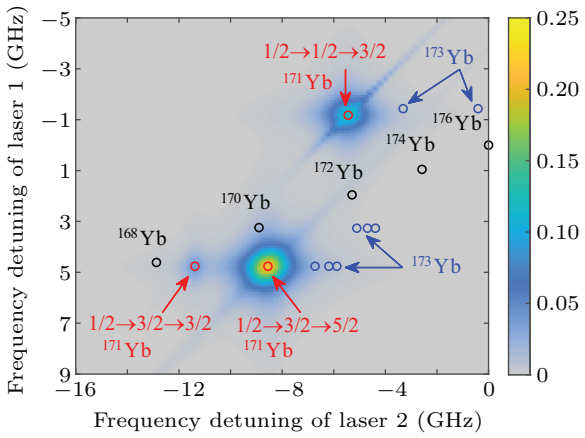


Fig. 7. Two-dimensional contour plot of ^{171}Yb ionization probability *versus* frequency detuning.

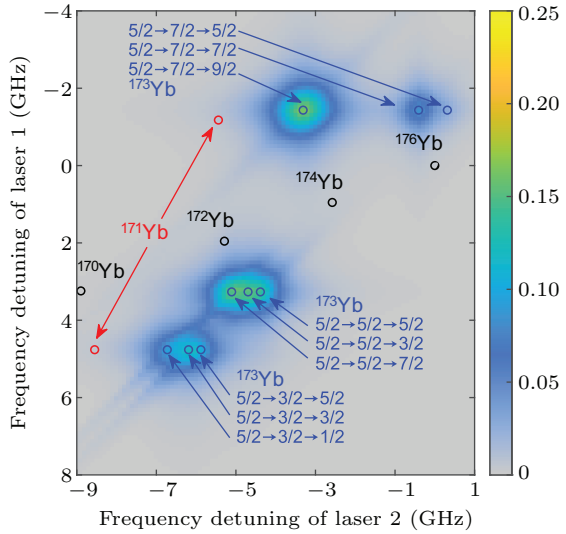


Fig. 8. Two-dimensional contour plot of ^{173}Yb ionization probability *versus* frequency detuning.

The second phenomenon is explained with the help of Fig. 9, which shows the peak ionization probabilities ordering among ^{176}Yb, ^{171}Yb, and ^{173}Yb under different laser power densities. It can be concluded from Fig. 5 that the ^{176}Yb and ^{171}Yb display the same ionization process under the hypothetical condition of zero hyperfine splitting. Therefore, total contributions to ionization probability of three transition paths in ^{171}Yb are equivalent to those of only one path in ^{176}Yb. Under the circumstances of real hyperfine splitting, the ionization probability of ^{171}Yb is lower than that of ^{176}Yb in the case of unsaturated excitation because the non-resonant transition paths make little contributions to the ionization probability for ^{171}Yb. However, contrary relation appears under supersaturated excitation conditions because of the power broadening effect of non-resonant transition paths in ^{171}Yb ionization processes. Therefore, it is unnecessary to increase laser bandwidths for higher ionization probability in odd isotope excitation process, and choosing appropriate transition path is a critical step.

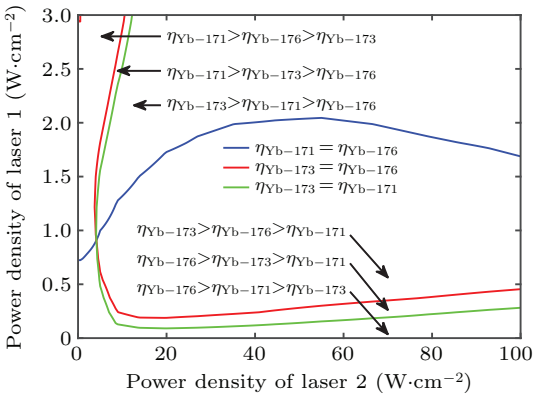


Fig. 9. Peak ionization probabilities ordering among ^{176}Yb, ^{171}Yb, and^{173}Yb under different laser power densities.

The total ionization yield and ^{176}Yb abundance are two most important indices in ^{176}Yb enrichment, the former is relevant to ionization probabilities and natural abundances of all isotopes, and the latter represents the photoionization selectivity of ^{176}Yb relative to other isotopes. To evaluate the final products of LIS process comprehensively, two-dimensional contour plots of these two indices *versus* frequency detuning are shown in Fig. 10, where the colorful circles have the same meanings as those in Figs. 6–8. The total yield shows its highest value around the resonant point of ^{174}Yb due to the high natural abundance and high ionization probability of ^{174}Yb isotope, while the ^{176}Yb abundance is unsatisfying in this area. The total yield can only be obtained about 3.2% when laser frequencies resonate with ^{176}Yb isotope. Because the central frequencies of other isotopes are almost located on the same side from the perspective of ^{176}Yb, the ^{176}Yb abundance in products rises distinctly on another side as shown in Fig. 10(b). Interestingly, there exists a strip domain where high ^{176}Yb abundance can be obtained in products because

of the two-photon coherent transition, while the viability and effectiveness need to be verified in experiments. Generally, resonant excitation with ^{176}Yb is an optimal choice from the standpoints of total ionization yield and ^{176}Yb abundance.

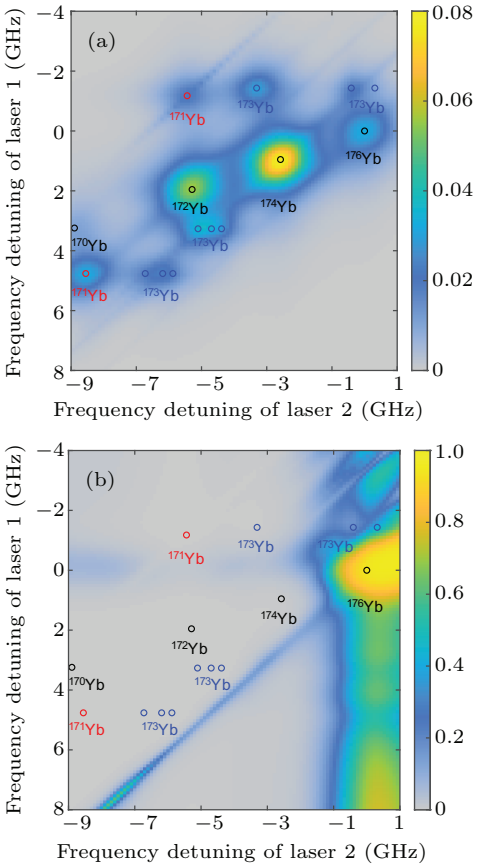


Fig. 10. Two-dimensional contour plots of (a) total ionization yield and (b) ^{176}Yb abundance *versus* frequency detuning.

3.3. Discussion of systematic parameters

In the ytterbium selective photoionization processes, laser parameters and atomic Doppler broadening play critical roles in determining the total ionization yield and target isotope abundance. It is known that the influences of laser time delay are equivalent to those of laser power density from our previous article.[25] The influences of laser frequency detuning have been discussed in Subsection 3.2. Therefore, it is important to identify the influences of other laser parameters (power density, bandwidth, polarization) and atomic Doppler broadening under the condition of resonant excitation with ^{176}Yb. In order to obtain the effects of a single parameter on ^{176}Yb enrichment, other parameters would use the benchmark values in Table 2 unless otherwise specified.

Figure 11 shows the abundances of ytterbium isotopes and total yield *versus* power density of two excitation lasers. For convenience, the saturated power densities of two lasers and their threefold values are denoted by dashed lines, and the corresponding abundances of ^{176}Yb are also marked. Power densities of laser 1 and laser 2 play similar roles qualitatively. With the increase of excitation power density, the total yield $P_{\rm ion}$ displays a rapid increase followed by a plateau. Because of the power broadening effect, ^{176}Yb abundance decreases monotonically and the abundances of other non-resonant isotopes increase monotonically within the simulation range. These two important indices are more sensitive to power density of laser 2 than that of laser 1. It is because laser frequency detuning of the second transition is larger than those of the first one, and the saturated excitation of the first transition requires smaller Rabi frequency generally for the non-resonant isotopes in this photoionization scheme.

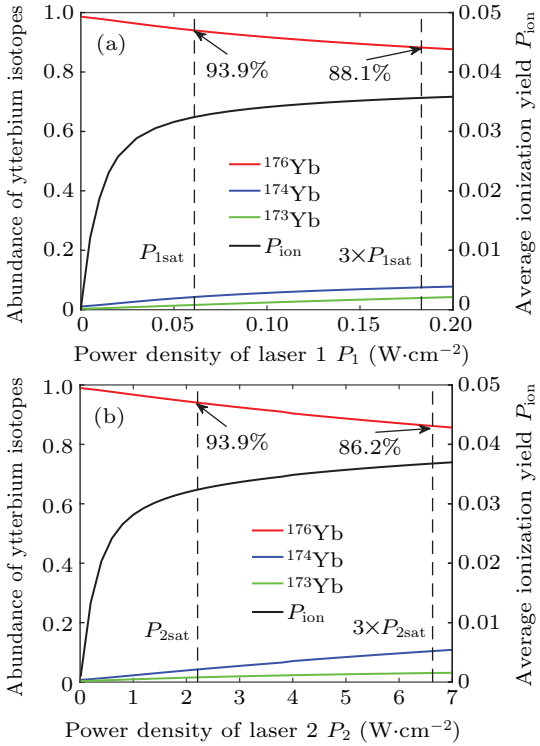


Fig. 11. Abundances of ytterbium isotopes and total yield *versus* power density of (a) laser 1 and (b) laser 2.

The influences of laser bandwidth, which is another critical parameter, are shown in Fig. 12. The influences of laser bandwidth show similar characteristics to those in Fig. 11, including the overall trends and differences between laser 1 and laser 2. Abundance of ^{176}Yb decreases monotonically with the increase of laser bandwidth, while those of ^{173}Yb and ^{174}Yb increase monotonically. It can be explained as follows. The spectral power density (SPD) at the resonant frequency (such as the central wavelength of ^{176}Yb for ^{176}Yb enrichment) displays a downward trajectory with the increase of bandwidth. As a result, the ionization probability of ^{176}Yb decreases monotonically. However, the SPD at non-resonant frequency (such as the central wavelength of ^{174}Yb) increases first and then decreases, and the ionization probabilities of non-resonant ytterbium isotopes display the similar tendencies. The turning points are positively correlated with the isotope shifts of non-resonant isotope relative to those of ^{176}Yb. As shown in Fig. 12(a), the abundance of ^{174}Yb is close to saturation when bandwidth of laser 1 approaches to the isotope

shift 0.954 GHz. Besides, the bandwidth of laser 2 has more significant influences on the abundances of ytterbium isotopes and total yield because of the same reasons illustrated in the previous subsections. With the consideration of high ^{176}Yb abundance, narrower bandwidths are required for excitation lasers.

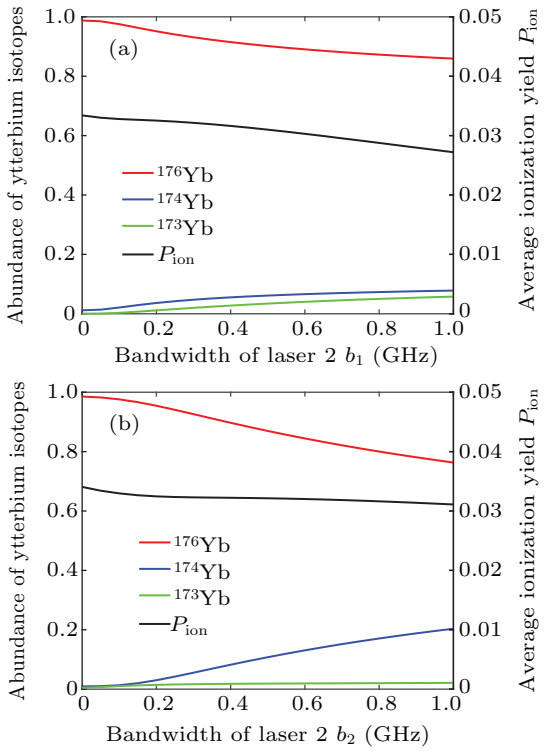


Fig. 12. Abundances of ytterbium isotopes and total yield *versus* bandwidths of (a) laser 1 and (b) laser 2.

Isotopic selectivity in LIS process is generally achieved from the isotope shift by using narrow bandwidth lasers, and another way is based on the atomic alignment induced by laser polarization[26]. Isotopes with hyperfine structures are allowed to be excited, while isotopes with zero nuclear spins are prohibited from being exited by choosing proper photoionization schemes and laser polarization combinations. Figure 13 shows the abundances of ytterbium isotopes and total yield *versus* linear polarization degree, in which the ratio of left circular component to right circular component is 1:1. The results indicate that the laser polarization has negligible effects on ^{176}Yb enrichment under this three-step photoionization scheme. Small fluctuations of P_{ion} and ^{176}Yb abundance appear with the change of linear polarization degree because there are some differences in effective dipole matrix elements at different polarization component ratios. To sum up, the laser polarization is not a critical parameter, and it is difficult to enhance ^{176}Yb abundance greatly by adjusting laser polarization ratio based on this photoionization scheme.

Atomic Doppler broadening, which can affect the ionization results, exists naturally because of the interatomic collisions and divergence of atomic vapors. Figure 14 shows the abundances of ytterbium isotopes and total yield *versus* FWHM of Doppler broadening, where the Gaussian profile is adopted for the Doppler shift distribution. Results indicate that Doppler broadening has negative influences on the selective photoionization effect. ^{176}Yb abundance and total yield decline monotonically with the increase of Doppler broadening, which is consistent with our previous study.[25] The explanation, which is similar to that for laser bandwidth, is not provided again.

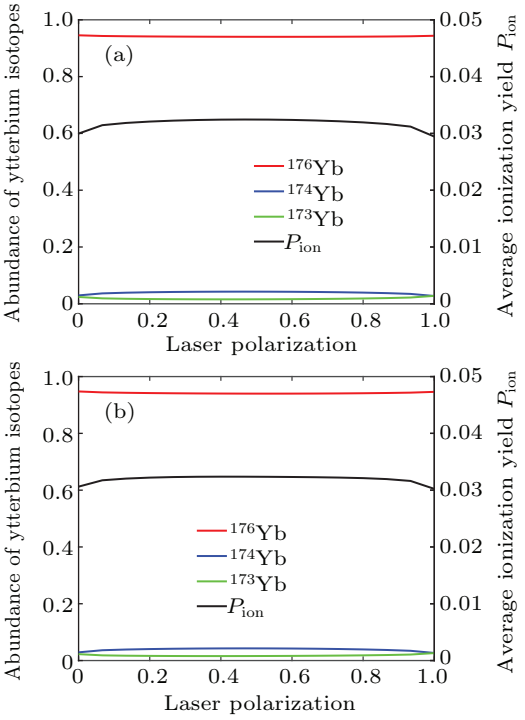


Fig. 13. Abundances of ytterbium isotopes and total yield linear polarization degree of (a) laser 1 and (b) laser 2.

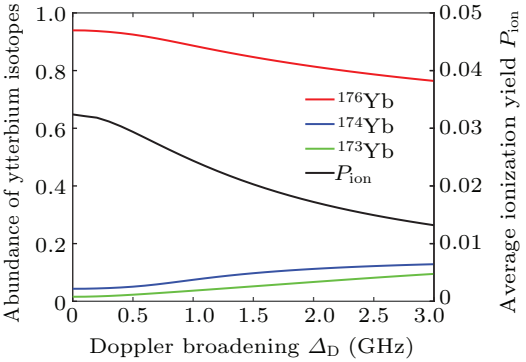


Fig. 14. Abundances of ytterbium isotopes and total yield *versus* Doppler broadening.

4. Conclusions

Three-step selective photoionization of ytterbium isotopes is investigated numerically through the density matrix theory. Apart from laser bandwidths and atomic Doppler broadening,[25] the hyperfine structures and magnetic sublevels are also taken into consideration. Numerical results are compared quantitatively with experimental results and they are in good agreements with each other for isotopic abundances in

a large range of total laser power density. In the present work, not only the excitation and ionization process of ytterbium is analyzed, but also the systematic parameters are optimized on this basis for ^{176}Yb enrichment. The Results show that the total yield and ^{176}Yb abundance cannot be enhanced simultaneously by adjusting excitation lasers' power density or frequency detuning individually. Extra-narrow excitation laser bandwidths and atomic Doppler broadening are necessary for high abundance of ^{176}Yb. Besides, laser polarization is found to have negligible influences on total yield and ^{176}Yb abundance. The physical model and numerically optimal results can provide semi-quantitative references for laser isotope separation of ytterbium.

References

[1] Chellan P and Sadler P J 2015 *Phil. Trans. R. Soc. A* **373** 20140182
[2] Yakovlenko S I 1999 *Russ. Phys. J.* **42** 732
[3] Babichev A P, Grigoriev I S and Grigoriev A I 2005 *Quantum Electron* **35** 879
[4] Yamabayashi H 1994 *Radioisotopes* **43** 296
[5] D'yachkov A B, Gorkunov A A and Labozin A V 2018 *Opt. Spectrosc* **124** 13
[6] Cutler C S, Smith C J and Ehrhardt G J 2000 *Cancer Biother. Radio.* **15** 531
[7] Fricker S P 2006 *Chem. Soc. Rev.* **35** 524
[8] Kostelnik T I and Orvig C 2019 *Chem. Rev.* **119** 902
[9] Dash A, Raghavan M and Pillai A 2015 *Nucl. Med. Mol. Imaging* **49** 85
[10] Banerjee S, Pillai M R A and Knapp F F 2015 *Chem. Rev.* **115** 2934
[11] Suryanarayana M V and Sankari M 2021 *J. Opt. Soc. Am. B* **38** 3331
[12] Suryanarayana M V 2021 *J. Opt. Soc. Am. B* **38** 353
[13] Vogel W V, Marck S C and Versleijen M W J 2021 *Eur. J. Nucl. Med. Mol. Imaging.* **48** 2329
[14] Borisov S K, Kuz'mina M A and Mishin V A 1996 *Russ. Laser Res.* **17** 332
[15] Yakovlenko S I 1998 *Quantum Electron* **28** 945
[16] Andreev O I, Derzhiev V I and Dyakin V M 2006 *Quantum Electron* **36** 84
[17] Park H, Kwon D H and Cha Y H 2008 *J. Nucl. Sci. Technol. Supplement* **6** 111
[18] Park H, Kwon D H and Cha Y H 2006 *J. Korean Phys. Soc.* **49** 382
[19] Rabi I I 1937 *Phys. Rev.* **51** 652
[20] Demtröder W 2008 *Laser Spectroscopy* Vol. 1 *Basic Principles*, 4th edn. (Berlin, Heidelberg: Springer-Verlag)
[21] Greenland P T 1990 *Contemp. Phys.* **31** 405
[22] Sankari M, Kumar P and Suryanarayana M 2008 *J. Opt. Soc. Am. B* **25** 1820
[23] Krynetskii B B, Mishin V A and Prokhorov A M 1991 *J. Appl. Spectrosc.* **54** 338
[24] Park H, Kostritsa S and Kwon D 2002 *J. Korean Phys. Soc.* **41** 322
[25] Lu X Y, Wang L D and Li Y F 2022 *Chin. Phys. B* **31** 063203
[26] Sahoo A C, Mandal P K and Shah M L 2017 *J. Phys. Commun.* **1** 055010